Acta Materialia 302 (2026) 121675

Contents lists available at ScienceDirect

Acta Materialia

journal homepage: www.elsevier.com/locate/actamat

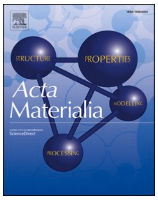

Achieving ideal hetero-lamella structure for superior strength–ductility in a medium-entropy alloy via engineering initial grain size

Shu-Yi Tung [a], Yi-Chia Chen [a], Yuntian Zhu [b], Ming-Hung Tsai [a,c,d,*]

[a] *Department of Materials Science and Engineering, National Chung Hsing University, Taichung, Taiwan*
[b] *Department of Materials Science and Engineering, City University of Hong Kong, Kowloon, Hong Kong, China*
[c] *Graduate Program in Semiconductor and Green Technology, Academy of Circular Economy, National Chung Hsing University, Nantou, Taiwan*
[d] *High Entropy Materials Center, National Tsing Hua University, Hsinchu, Taiwan*

ARTICLE INFO

Keywords:
Mechanical properties
Microstructure
Grain size
Nucleation and growth
Heterostructured materials

ABSTRACT

The hetero-lamella (HL) structure, featuring thin, uniformly distributed lamellar soft-zones embedded in a hard matrix, is widely regarded as the ideal architecture for maximizing heterostructure effect, as measured by hetero-deformation induced (HDI) stress. However, conventional rolling–recrystallization processes often fail to realize ideal HL structure due to the uncontrolled nature of recrystallization. Here, we propose a new strategy to alter the recrystallization behavior by refining the initial grain size before the R-R process. Implemented via a dual-stage thermomechanical treatment, this approach transforms a coarse, irregularly banded heterostructure into a near-ideal HL structure with fine ($\sim 20 \times 8\ \mu m^2$), uniformly spaced (inter-zone spacing $\sim 10\ \mu m$) soft-zones and enhanced interfacial density. Applied to a VCoNi medium-entropy alloy, this architecture achieves a yield strength of 1.36 GPa, an ultimate tensile strength of 1.61 GPa, and a uniform elongation exceeding 27 %. Moreover, our study reveals that hard-zone thickness critically influences heterostructure effectiveness at high strain, with thinner hard-zones lose strain incompatibility early, weakening HDI hardening. This is the first direct experimental evidence that the function of hetero-interface is influenced by hard-zone morphology. This work offers a new strategy to realize ideal heterostructures and thus opens new opportunities for developing next-generation heterostructured alloys with unprecedented combinations of strength and ductility.

1. Introduction

Heterostructured materials (HSMs) have attracted extensive attention because of their potential to overcome the longstanding strength–ductility trade-off that limits the performance of conventional metallic materials [1–3]. By deliberately incorporating microstructural heterogeneity—typically in the form of variations in grain size, dislocation density, or phase constitution—HSMs create mechanically distinct soft- and hard-zones that interact strongly during plastic deformation. The resulting incompatibility in deformation behavior generates pronounced strain gradients near hetero-zone boundaries, which in turn induce the accumulation of geometrically necessary dislocations (GNDs) and the development of long-range internal stresses, commonly referred to as back stress and forward stress. Such internal stresses and excess GNDs give rise to hetero-deformation-induced (HDI) strengthening and strain hardening. As a result, HSMs exhibit exceptional combinations of strength and ductility that far exceed those achievable in their homogeneous counterparts [4,5].

To achieve optimal mechanical performance in HSMs, careful design of the soft- and hard-zone architecture is essential. The volume fraction, size, morphology, and spatial distribution of the constituent zones must be optimized to maximize HDI effects and enable a superior strength–ductility synergy. Based on theoretical analyses and experimental observations [2–4,6], the following design principles are widely recognized: First, soft-zones should occupy a minority of the total volume to make sure they are well-constrained by the surrounding hard matrix. A lower soft-zone fraction prevents plastic percolation and enhances mechanical confinement, both of which are crucial for maintaining strain incompatibility and promoting HDI effects. Second, soft-zones should be small and their morphology should be near-lamella. Reducing soft-zone size increases the zone boundary density (per unit volume of soft-zone). Since strain gradients and GND accumulation are most active near zone boundaries, this amplifies the HDI effects. Lamellae or other high-aspect-ratio morphologies can

---

[*] Corresponding author at: Department of Materials Science and Engineering, National Chung Hsing University, Taichung, Taiwan.
E-mail address: mhtsai@nchu.edu.tw (M.-H. Tsai).

https://doi.org/10.1016/j.actamat.2025.121675
Received 19 August 2025; Received in revised form 22 October 2025; Accepted 24 October 2025

further maximize the surface-to-volume ratio of the soft-zones. Third, the thickness of the soft-zones should be optimized. Both modeling and experiments suggest that the most effective soft-zone thickness is approximately twice the width of the hetero-boundary affected region (HBAR), which typically ranges from 2 to 4 μm in FCC alloys [4,7–9]. This translates to a best soft-zone thickness of several micrometers. Fourth, soft-zones should be uniformly dispersed within the hard matrix and spacing between them should not be too large. This arrangement encourages the activation of distributed, multi-directional shear bands rather than a single dominant shear path. Such dispersive shear bands enhances plastic stability and delays the onset of failure, thereby improving overall ductility [10,11].

The above design principles establish the hetero-lamella (HL) structure as one of the most effective configurations among HSMs [2,12]. An ideal HL structure consists of 20–30 % thin, spatially discrete lamellar soft-zones uniformly embedded within a continuous hard matrix [2]. Ideally, the soft-zones should be only several micrometers thick but closely spaced to each other. Such a configuration ensures high interfacial area, enhances strain incompatibility, and fully activates HDI mechanisms. Extensive efforts have been made to realize such HL architectures, primarily through two types of processing routes. The first involves powder-based processing [13–16]. For example, powder thixoforming offers excellent controllability over lamellar geometry and the soft-/hard-zone fractions by adjusting the semi-solid temperature and holding time. This high degree of microstructural tunability enables the formation of uniform, well-aligned lamellae that closely resemble an ideal heterogeneous configuration. By varying these processing parameters, Wang et al. achieved alternating coarse- and fine-grained lamellae with controlled soft-/hard-zone ratios of approximately 3:7 to 4:6 and lamellar thicknesses of 10–30 μm, resulting in an outstanding strength–ductility synergy [13]. Nevertheless, the dependence on powder metallurgy evidently limits cost efficiency, scalability, and attainable sample size.

The second and more widely adopted route is the rolling–recrystallization (R–R) process. R–R is industrially scalable, compatible with conventional metal-forming technologies, and has therefore been extensively investigated in recent years [17–22]. For instance, Jiang et al. developed alternating coarse- and fine-grained lamellae in an Al–Zn–Mg–Cu alloy through gradient-temperature rolling followed by aging, achieving an improved strength–ductility synergy via enhanced strain partitioning and precipitation-assisted HDI strengthening [21]. Likewise, Liu et al. demonstrated that 90 % cold rolling followed by partial recrystallization at 700–800 °C in an N-doped CrCoNi medium-entropy alloy produced a HL architecture exhibiting an excellent combination of high yield strength (∼1.0–1.3 GPa) and superior fracture toughness [22]. Despite these encouraging results, the R–R process rarely yields the ideal HL configuration. The microstructures obtained are typically composed of large, irregularly shaped soft and hard zones—often hundreds of micrometers in length and tens of micrometers in width—with random spacing and non-uniform morphology [23–26]. Such pronounced deviations from the ideal lamellar geometry prevent R–R-processed materials from fully realizing their mechanical potential.

The limited capability of the R–R process to produce ideal HL structure stems from the fact that the formation of heterostructures in this route is governed by spontaneous recrystallization phenomena—primarily nucleation and growth along various deformation-induced features. These processes are highly sensitive to local microstructural fluctuations that occur naturally, and are inherently difficult to control with precision [27]. Although macroscopic processing parameters—such as annealing temperature and duration, rolling reduction, and rolling temperature—can influence overall recrystallization behavior to some extent, they lack the spatial resolution and selectivity required to finely regulate critical features such as the size, morphology, and spatial distribution of the resulting soft- and hard-zones [28–31]. As a result, tuning these macroscopic parameters may allow for approximate adjustment of the soft-/hard-zone volume fraction, but offers virtually no control over soft-zone size or uniformity.

To realize an ideal HL structure, a new strategy is required—one that fundamentally alters the recrystallization behavior rather than allowing it to be dictated by random local microstructural inhomogeneities. In this study, we demonstrate that tailoring the initial microstructure of the material—particularly its grain size—can serve as a key design strategy for enabling HL structure formation. Specifically, refining the initial grain size transforms the originally coarse, irregularly banded heterostructure into a near-ideal HL structure. The resulting microstructure features significantly smaller soft-zones (∼20 × 8 μm^2) and markedly improved spatial uniformity, with inter-zone spacing reduced to ∼10 μm—characteristics that are otherwise extremely difficult to achieve through conventional processing. This paradigm shift arises from the refinement of the initial grain size, which increases the grain boundary density by several hundred times. This drastic change alters the dominant mechanism governing the distribution of recrystallization nucleation sites, which in turn reshapes the overall recrystallization behavior and the final heterostructure. We validate this approach in a VCoNi medium-entropy alloy by introducing a pre-processing step prior to the regular thermomechanical treatment (TMT) in the R–R process, thereby creating a dual-stage thermomechanical treatment (DS-TMT). The VCoNi alloy, in its single-phase FCC state, already offers a good strength–ductility balance [32–34]. During intermediate-temperature annealing, κ-phase particles precipitate and provide additional strengthening [35–37]. Compared to the conventional TMT route, the DS-TMT-processed VCoNi alloy exhibits significantly improved mechanical performance, achieving a yield strength (YS) of 1.36 GPa, an ultimate tensile strength (UTS) of 1.61 GPa, and a uniform elongation (UEL) exceeding 27 %. Beyond microstructure and properties, this study also uncovers a critical but underexplored factor in heterostructure design: the geometry of the hard-zones. Specifically, we find that boundaries adjacent to thinner hard-zones lose their ability to sustain strain incompatibility and accumulate GNDs at higher strains, leading to the degradation of HDI effects.

2. Experimental procedures

VCoNi alloys were fabricated by vacuum arc melting under a high-purity argon atmosphere. Elemental raw materials with purities of 99.95 % or higher were melted in a water-cooled copper crucible and remelted four times to enhance chemical homogeneity. To investigate the influence of initial grain size on the microstructural evolution, two thermomechanical processing routes were employed: a regular thermomechanical treatment (TMT) and a dual-stage thermomechanical treatment (DS-TMT), as schematically illustrated in Fig. 1a and b. For the TMT route, as-cast ingots (dimensions: 50 × 25 × 8 mm^3) were first homogenized in vacuum at 1200 °C for 24 h. Homogenized ingots then underwent a single-stage thermomechanical treatment (referred to as the main-processing step), which involved cold rolling to a final thickness of 1 mm (87.5 % reduction) followed by annealing in air at various temperatures for 5 minutes. The resulting specimens are hereafter referred to as TMT samples. For the DS-TMT route, thicker ingots (50 × 25 × 16 mm^3) were used to enable an additional pre-processing step designed to refine the initial grain size. These thick ingots were homogenized under the same conditions (1200 °C for 24 h), followed by 50 % cold rolling and full recrystallization at 1000 °C for 10 minutes. This pre-processing yielded a fine-grained microstructure prior to the main-processing step. Subsequently, the pre-processed ingots were subjected to the same cold rolling and annealing procedures as those used for the TMT route. The final specimens obtained via this two-step treatment are referred to as DS-TMT samples.

Microstructural analysis was performed using a JEOL JSM-7800F scanning electron microscope (SEM). Crystal structure analysis was performed using a BRUKER-D8 Discover X-ray diffractometer operating at 40 kV and 30 mA using Cu Kα radiation. Electron backscatter

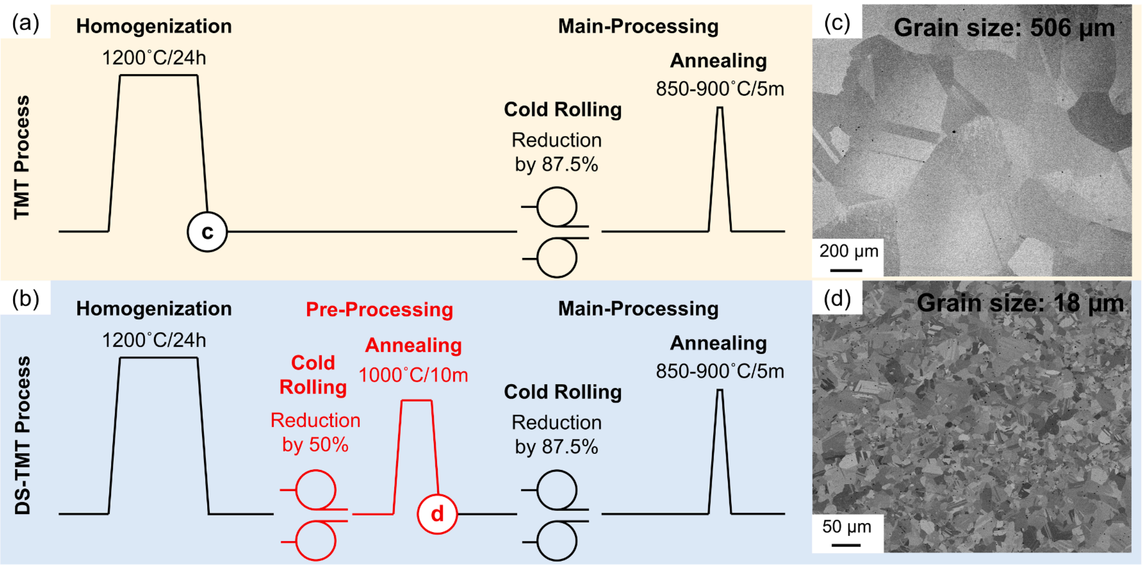

Fig. 1. (a and b) Schematic illustration of the two thermomechanical processing routes. (c)(d) Microstructures of the TMT and DS-TMT samples before entering the main processing step.

diffraction (EBSD) was carried out with an Oxford NordlysMax 3 system mounted on a JEOL JSM-7800F SEM. Prior to observation, all specimens were mechanically polished using standard metallographic techniques. Transmission electron microscopy (TEM) investigations were conducted on a JEOL JEM-2100F microscope. TEM foils were mechanically thinned to below 100 μm and subsequently twin-jet polished in an electrolyte mixture of 5 % perchloric acid and 95 % ethanol.

Tensile test samples were cut to gauge dimensions of 16 × 4 × 1 mm^3 and tested with a Shimadzu AGS-1000kN universal tensile machine with a strain rate of 1 × 10^{-3} s^{-1}. Tensile specimens were wire-cut from the rolled sheet such that their longitudinal axis was parallel to the rolling direction (RD), and tensile tests were performed along the same direction. A series of loading–unloading–reloading (LUR) tests were conducted, with a strain rate of 5 × 10^{-4} s^{-1} applied during loading and reloading, and a load-controlled unloading rate of 3.3 N/s down to a minimum load of 200 N. Nanoindentation tests were carried out to evaluate local mechanical properties across different microstructural regions. A Bruker Hysitron TI 980 TriboIndenter equipped with a Berkovich diamond tip was used, with a peak load of 12 mN applied at a loading rate of 1 mN/s. EBSD scans were performed after indentation to identify the precise location and type of each indent. Indentation data near indistinct zone boundaries were excluded, and at least 50 valid measurements were taken from each clearly defined region.

3. Results

3.1. Initial microstructure with and without pre-processing

To clarify the effect of the pre-processing, the initial microstructures prior to the main-processing step are compared for the TMT and DS-TMT routes. Figs. 1c and 1d show the as-homogenized (As-Homo) and pre-processed states of the two samples, respectively. The As-Homo specimen contains large equiaxed grains with occasional annealing twins, and an average grain size of approximately 506 μm (Fig. 1c). In contrast, the pre-processed state in the DS-TMT specimen shows a fully recrystallized microstructure characterized by a significantly refined grain size of ~18 μm (Fig. 1d) and a somewhat higher density of annealing twins. SEM observations and XRD analysis (Fig. S1) confirm the absence of secondary phases in both cases, verifying that both samples retain a single-phase FCC structure. Therefore, the major microstructural distinction between the two samples prior to main-processing lies in their markedly different grain sizes.

3.1. Mechanical properties

Fig. 2a presents the engineering stress–strain curves of the VCoNi alloys, with key mechanical parameters summarized in Table 1. The TMT samples already demonstrate excellent mechanical performance. For example, the TMT sample annealed at 875 °C for 5 minutes (TMT-875) achieves a YS of 1044 MPa and an UTS of 1473 MPa, while retaining a high UEL of 31 %. In contrast, the DS-TMT route, designed to refine initial grain size, significantly enhances strength with only a marginal compromise in ductility. Specifically, the DS-TMT-875 sample demonstrates a YS of 1359 MPa and a UTS of 1612 MPa, reflecting increases of 315 MPa and 139 MPa, respectively, compared to TMT-875 (Fig. 2b). Notably, at such high strength levels, substantial strength gains typically lead to significant ductility losses. However, the DS-TMT-875 sample maintains a high UEL of 27 %, a reduction of only 4 % relative to TMT-875.

A similar trend is observed in the annealing at 900 °C. Compared to TMT-900, DS-TMT-900 again shows a substantial strength enhancement: the YS increases by 217 MPa, and the UTS increases by 121 MPa. Despite this considerable strengthening, the UEL in DS-TMT-900 remains high at 32.5 %, representing a reduction of only 2.9 %. These results clearly demonstrate that the DS-TMT route significantly boosts mechanical strength with minimal sacrifice in ductility, highlighting its effectiveness in optimizing the strength–ductility synergy of HSMs even at high-strength regimes where such trade-offs are typically unavoidable.

To investigate the effect of initial grain size on strain hardening behavior, TMT and DS-TMT samples exhibiting the best mechanical performance are selected for comparison, and their corresponding hardening behaviors are shown in Fig. 2c. Both TMT-875 and DS-TMT-875 exhibit discontinuous yielding, indicating the activation of the HDI effect. These samples also show sustained strain hardening until meeting the Considère criterion for necking. Notably, refining the initial grain size does not harm the strain hardening capacity; as a result, DS-TMT-875 maintains the ductility level of TMT-875 despite having a much higher yield strength.

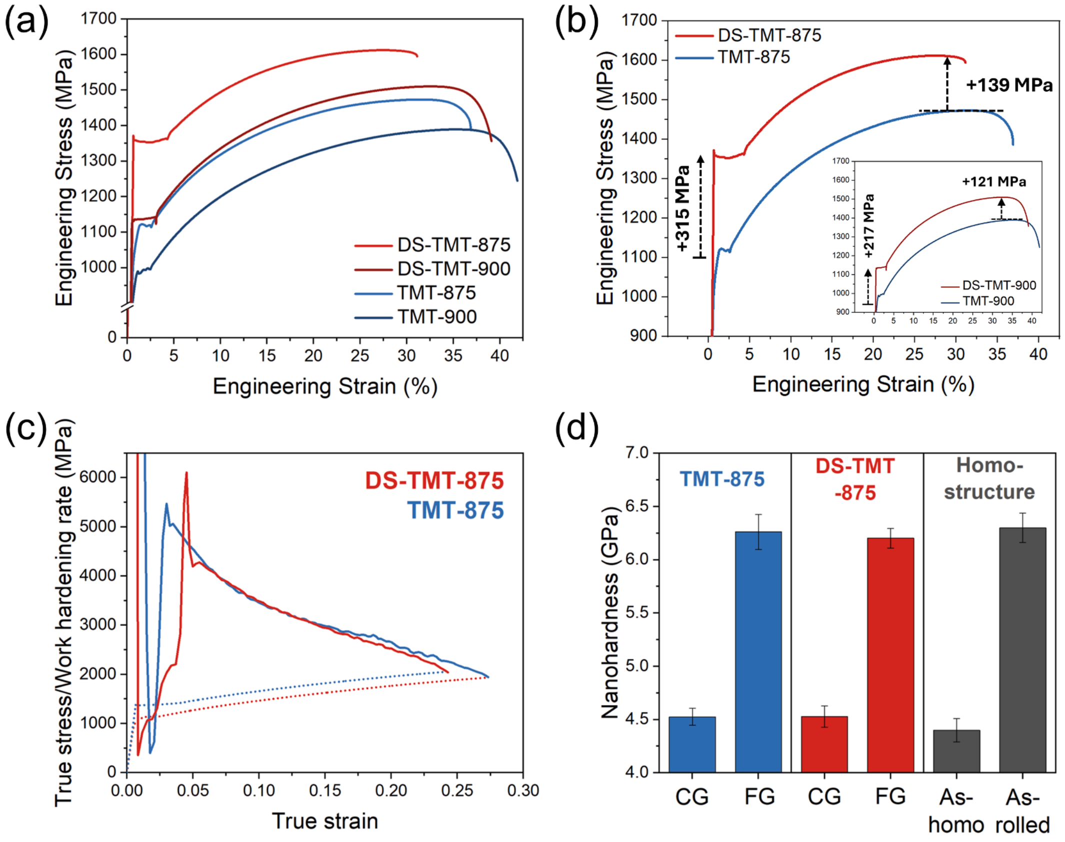

Fig. 2. (a) Engineering stress–strain curves of samples processed by different routes and annealing temperatures; (b) Enlarged comparison of DS-TMT and TMT samples annealed at 875 °C and 900 °C (inset), respectively, illustrating the strength improvements due to initial grain size refinement; (c) Work-hardening rate and true stress as functions of true strain for TMT-875 and DS-TMT-875; (d) Nanohardness values of CG and FG regions in TMT-875 and DS-TMT-875, compared with those of homogeneous As-homogenized and As-rolled alloys.

Table 1

Tensile properties of the VCoNi alloys under different processing conditions.

Processing route	Anneal. temp. (°C)	YS (MPa)	UTS (MPa)	UEL (%)	EL (%)
TMT	875	1044 ± 20	1473 ± 21	31.3 ± 0.3	36.9 ± 0.6
	900	914 ± 12	1389 ± 34	35.4 ± 2.4	41.9 ± 2.8
DS-TMT	875	1359 ± 10	1612 ± 26	27.1 ± 0.6	31.2 ± 1.0
	900	1131 ± 25	1510 ± 19	32.5 ± 1.3	39.1 ± 1.7

3.2. *Microstructural characterization*

The microstructure of the TMT-875 sample is revealed in Fig. 3. As shown in the low-magnification EBSD images (Figs. 3a and b), the TMT-875 sample exhibits an alternating banded structure consisting of coarse-grained (CG) and fine-grained (FG) bands. These bands are typically hundreds of micrometers long and tens of micrometers wide, but can vary significantly. Notably, FG sub-bands are often observed within the CG bands. Both the FG bands and FG sub-bands are hereafter collectively referred to as FG regions. According to image-based quantification (Table 2), the CG and FG regions occupy approximately 65 % and 35 % of the total volume, respectively. Their spatial configuration is illustrated schematically in Fig. 3c. XRD analysis confirms a single-phase FCC matrix with a minor fraction of κ-phase precipitates in the TMT-875 sample (Fig. S1c). The κ phase, identified as $(Co,Ni)_3V$, is an A_3B-type rhombohedral intermetallic (*h*R36-$BaPb_3$, SG No. 166) with a 9R-type close-packed stacking sequence (ABCBCACAB) [38,39]. This phase is known to precipitate in VCoNi alloys during intermediate-temperature annealing [40].

Figs. 3d–f show that the CG region in TMT-875 primarily consists of FCC grains (~95 %) with a minor fraction of κ-phase precipitates (~5 %), and exhibits a grain size of 7.8 μm (FCC phase). In contrast, the FG regions, including both the FG bands and FG sub-bands, contain a two-phase ultrafine structure composed of FCC grains and κ-phase particles (Fig. 3g–i), with an effective FCC grain size of only ~0.8 μm. Although EBSD cannot accurately resolve phase fractions in such fine structures, qualitative contrast and later TEM analysis (Fig. 5) indicate a significantly higher κ-phase volume fraction in the FG regions compared to the CG regions. Therefore, the difference between CG and FG regions lies not only in grain size but also in phase constituents.

Following initial grain refinement via the DS-TMT route, the overall microstructure becomes markedly finer, and the morphological arrangement of the CG/FG-region is fundamentally transformed. As shown in Fig. 4a–c, the DS-TMT-875 sample exhibits an inverted microstructural architecture compared to TMT-875: FG regions now constitute the continuous matrix, while CG lamellae are discretely embedded within it. According to Table 2, the volume factions of FG and CG regions are approximately 65 % and 35 %, respectively—essentially the reverse of those in the TMT-875 sample. This inverted architecture resembles the ideal HL structure, where soft-zones are constrained within a continuous hard-zone matrix to maximize HDI effects [12]. Additionally, unlike TMT-875, FG sub-bands are no longer found within the CG lamellae of DS-TMT-875. Despite significant morphological changes, the phase constituents within the CG/FG regions remain similar between the two samples. Figs. 4d–f show that the CG lamellae in DS-TMT-875 consist predominantly of FCC grains (98 %), with a minor presence of κ particles (2 %). The FG matrix also retains an

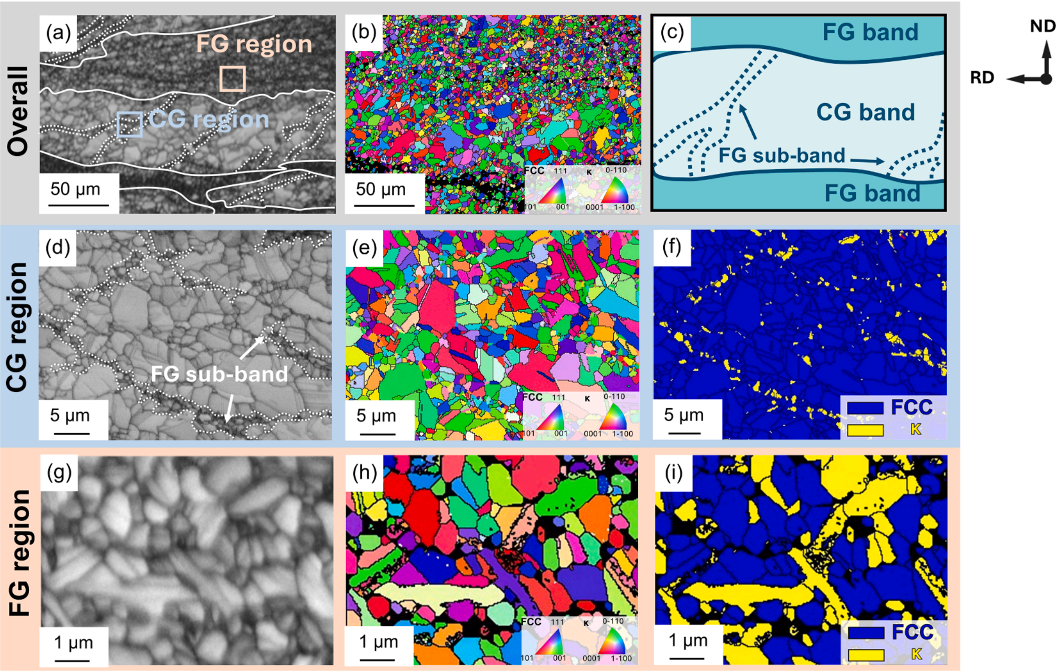

Fig. 3. EBSD analysis of the TMT-875 sample. (a–c) Low-magnification overview: (a) Band contrast image, (b) IPF_Z map, and (c) schematic of CG/FG band structure. (d–f) CG region: (d) Band contrast image, (e) IPF_Z map, and (f) phase map. (g–i) FG region: (g) Band contrast image, (h) IPF_Z map, and (i) phase map.

Table 2
Summary of microstructural parameters for the TMT-875 and DS-TMT-875 samples, including volume fraction of each region (V_r), volume fractions of the FCC and κ phases within each region (V_{FCC} and V_κ), and the effective grain size of the FCC phase (d_{eff}). Phase volume fractions in FG regions were obtained via TEM due to the insufficient spatial resolution of EBSD.

Sample	Region	Microstructural parameter			
		V_r (%)	V_{FCC} (%)	V_κ (%)	d_{eff} (µm)
TMT-875	CG	64.8 ± 1.7	95.2 ± 1.3	4.8 ± 1.3	7.8 ± 1.5
	FG	35.2 ± 1.7	64.1 ± 2.3	35.9 ± 2.3	0.8 ± 0.2
DS-TMT-875	CG	34.6 ± 2.2	98.0 ± 0.8	2.0 ± 0.8	2.7 ± 0.6
	FG	65.4 ± 2.2	71.3 ± 2.0	28.7 ± 2.0	0.9 ± 0.1

ultrafine-grained two-phase structure, and a higher κ fraction (Figs. 4g–i), similar to the FG regions in TMT-875. Again, due to EBSD resolution limitations, precise quantification of phase fractions within the FG regions is carried out via TEM later. An important difference between the two samples is that the average FCC grain size in the CG region of DS-TMT is only 2.7 µm—substantially finer than that observed in TMT-875 (7.8 µm).

To further investigate the microstructure in the FG regions, TEM analysis was conducted on both samples (Fig. 5). As shown in Figs. 5a–b, the FG regions in the two samples exhibit similar microstructures, featuring mostly dual-phase grains (where plate-shaped κ-phase plates precipitated coherently within FCC grains, often penetrating across the FCC matrix) and accompanied by occasional isolated κ particles. Quantitative TEM analysis (Table 2) reveals that the κ-phase volume fraction is slightly higher in TMT-875 (36 %) than in DS-TMT-875 (29 %). A representative dual-phase grain from TMT-875 is shown in Fig. 5c, where the selected area diffraction pattern (SADP, Fig. 5d) confirms a well-defined orientation relationship: $<110>_{FCC}$ // $<110>_\kappa$ and $\{111\}_{FCC}$ // $\{0009\}_\kappa$. This crystallographic alignment indicates a fully coherent interface, as further verified by high-resolution TEM imaging (Fig. 5e-f). EDS analysis confirms that the κ phase is Co-rich and contains substantial Ni, consistent with a $(Co,Ni)_3V$ stoichiometry (Table S1). Notably, unlike conventional brittle intermetallics, these κ precipitates are deformable to some extent due to their coherent interfaces [35,36]. This allows them to act as strengthening features without initiating early failure, thereby contributing to the observed balance of strength and ductility.

3.3. Hetero-zones and global HDI stress

Based on previous microstructural characterization, the CG and FG regions exhibit clearly distinct phase constituents and structures. In order to understand the strength contrast between CG and FG regions in TMT-875 and DS-TMT-875, nanoindentation measurements were conducted (Fig. 2d). For comparison, homogeneous samples—the As-Homo and the As-Rolled alloys—were also examined. The CG regions in both HSM samples exhibit similar nanohardness (~4.5 GPa), comparable to As-Homo alloy (~4.4 GPa). Likewise, the FG regions show nearly identical values (~6.3 GPa), similar to As-Rolled alloy. Notably, the As-Homo and As-Rolled alloys differ in YS by a factor of 3.7 (Table S2), supporting the classification of CG and FG regions as soft- and hard-zones, respectively, and confirming the classification of both samples as heterostructures.

Because HDI mechanisms play a pivotal role in HSMs, the level of HDI stress provides critical insight into their mechanical performance [5]. Fig. 6a shows the true stress–strain curves of TMT-875, and DS-TMT-875 obtained via LUR tests. Both samples exhibit clear reverse plastic hysteresis, suggesting non-uniform deformation. Fig. 6b clearly displays visible hysteresis loops for both samples, highlighting the non-uniform deformation and the operation of HDI mechanisms. The HDI stress (σ_{HDI}) is estimated from each loop using the equation [41]:

$$\sigma_{HDI} = \frac{\sigma_r + \sigma_u}{2},$$

where σ_r and σ_u are the reloading and unloading yield stresses, respectively. σ_{HDI} represents the collective effect of back and forward stress. However, at the yield point it can be regarded as back stress since the hard zones are still largely elastic [42]. As shown in Fig. 6c, at low strains (<10 %), both samples display similar HDI stress increments, indicating comparable HDI strain hardening behavior during early stage of deformation. However, beyond 10 % strain, a divergence emerges:

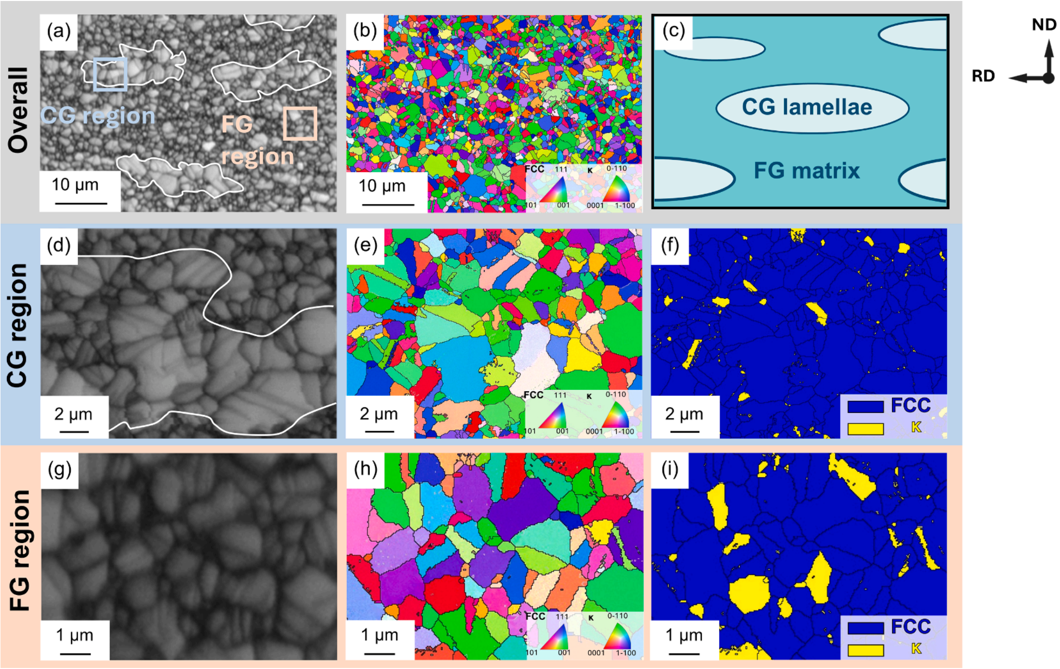

Fig. 4. EBSD analysis of the DS-TMT-875 sample. (a–c) Low-magnification overview: (a) Band contrast image, (b) IPF_Z map, and (c) schematic of the CG lamella and the FG matrix. (d–f) CG region: (d) Band contrast image, (e) IPF_Z map, and (f) phase map. (g–i) FG region: (g) Band contrast image, (h) IPF_Z map, and (i) phase map. Note: The phase map in FG region is inaccurate due to EBSD resolution; TEM analysis is employed later for precise quantitative assessment.

DS-TMT-875 maintains a steady rate of HDI stress increase, whereas TMT-875 exhibits a noticeable reduction in slope. This suggests a partial loss of HDI strain hardening in TMT-875 at higher strain. In contrast, DS-TMT-875 retains robust HDI effects throughout deformation.

3.4. Local HDI stress: Unequal efficacy of different zone boundary types

Since HDI effects in HSMs primarily originate from HBARs, the partial loss of HDI strain hardening observed in TMT-875 (see Sec. 3.4) implies a degradation of HDI effects at certain boundaries. To better understand this phenomenon, it is essential to examine the local mechanical response at individual zone boundaries. Given that GNDs mainly accumulate on the soft-zone side of a hetero-interface, kernel average misorientation (KAM) line scans were performed from the zone boundaries into adjacent coarse grains to probe the local HDI response at the individual boundary level (Figs. 7a and b). According to the microstructural features shown in Fig. 3, the TMT-875 sample contains two types of hard-zones: Type I, large FG bands (denoted as HZ1), and Type II, FG sub-bands embedded within the CG band (denoted as HZ2). Accordingly, their respective zone boundaries are defined as ZB1 and ZB2. In contrast, the DS-TMT-875 sample (Fig. 4) contains only a single type of hard-zone and a corresponding zone boundary. They will be denoted as HZ3 and ZB3, respectively.

Figs. 7c and d present the measured GND accumulation profiles ahead of each zone boundary at strain levels of 3 % and 10 %, with regular grain boundaries (GBs) included as a baseline. At 3 % strain in TMT-875, both ZB1 and ZB2 exhibit higher KAM values than GBs, indicating stronger local HDI effects near zone boundaries. However, at 10 % strain, the KAM level near ZB1 continues to increase, while that near ZB2 remains largely unchanged and becomes comparable to GBs. This suggests that ZB2 loses its HDI effect at higher strain, as its capacity to accumulate GNDs becomes similar to that of an ordinary grain boundary. This trend is consistent with the reduced HDI slope observed in TMT-875 beyond 10 % strain (Fig. 6c). In contrast, the DS-TMT-875 sample shows sustained HDI activity across the two strain levels. As shown in Figs. 7e–f, the KAM level ahead of ZB3 consistently remains higher than that ahead of GBs at both 3 % and 10 % strain, indicating persistent strain incompatibility and HDI strengthening throughout deformation.

To understand the origin of the degraded HDI effect near ZB2 in TMT-875, TEM analysis was performed on samples strained to 10 %. As shown in Fig. 8a, the soft-zone contains high densities of dislocations and slip bands, indicative of extensive plastic deformation. In contrast, HZ1 shows markedly lower defect density (Fig. 8b), consistent with the expected strain partitioning behavior in HSMs, where hard-zones undergo less strain than adjacent soft-zones. Surprisingly, however, HZ2 contains pronounced planar slip and densely packed slip bands (Fig. 8c), resembling the deformation characteristics of soft-zones rather than hard-zones. This indicates that, despite both being classified as hard-zones, HZ1 and HZ2 exhibit markedly different deformation behavior at high strains. Additional differences are observed at their respective interfaces. As shown in Fig. 8d, instances of slip band propagation across ZB2 are visible, suggesting local breakdown of deformation confinement. In contrast, no such propagation is observed across ZB1. These observations collectively indicate that ZB2 is less effective in sustaining strain incompatibility, likely contributing to the decline in HDI strain hardening in TMT-875 at higher strain. The implications of the distinct deformation behaviors and boundary characteristics of HZ1 and HZ2 will be further discussed in the next section.

4. Discussion

4.1. How initial grain size influences heterostructure formation

As shown previously, the deliberate refinement of the initial grain size prior to the R–R process is a powerful strategy that transforms the microstructure from an alternating banded architecture with coarse bands—hundreds of micrometers in length and tens of micrometers in width—into one that closely matches the hetero-lamella (HL) structure design concept. This adjustment produces four major features:

(1) Increased hard-zone fraction (from 35 % to 65 %);
(2) Refined overall grain size (from 5.4 μm to 1.5 μm);

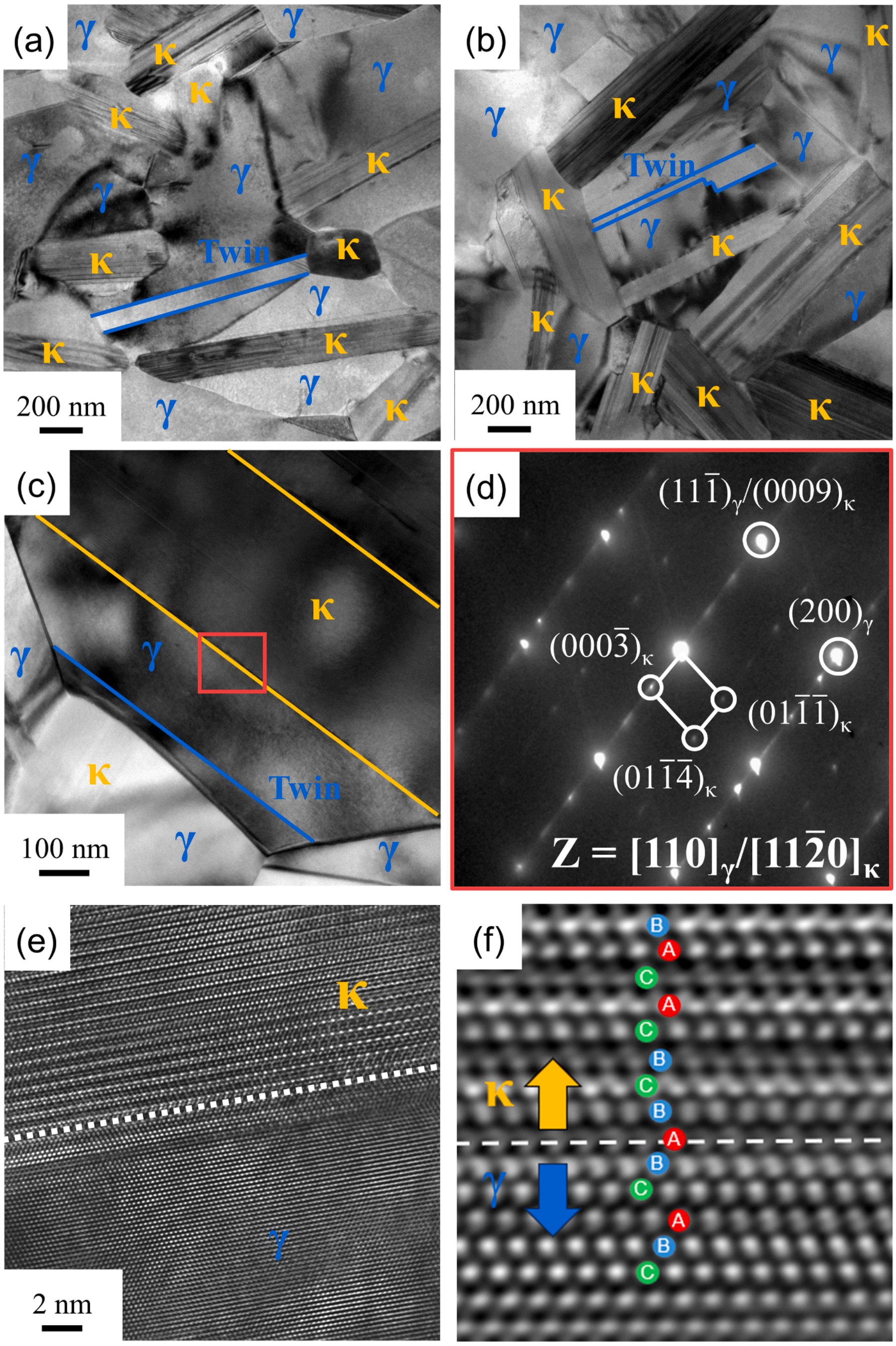

Fig. 5. (a and b) Low-magnification TEM images of (a) TMT-875 and (b) DS-TMT-875. (c) A dual-phase grain (FCC + κ) in the FG matrix of DS-TMT-875. (d) SADP obtained from the FCC/κ interface region highlighted in (c). (e) HR-TEM image of the FCC/κ phase interface. (f) Inverse fast Fourier transform (IFFT) image pattern derived from (e), highlighting the atomic stacking sequence and lattice coherency across the FCC/κ interface.

(3) Substantial reduction in soft-zone size (from ~300 × 100 μm^2 to ~20 × 8 μm^2);
(4) Improved soft-zone uniformity (inter-soft-zone spacing reduced from ~100 μm to ~10 μm)

Among these, (3) and (4) represent the most challenging requirements in ideal HL structure design and are almost unattainable by conventional strategies. Therefore, these changes collectively demonstrate the effectiveness of our strategy in realizing the critical geometric and spatial attributes of the HL structure.

The core of our strategy lies in the deliberate control of the nucleation-site distribution mechanism. This mechanism determines the density of recrystallization nuclei and, consequently, dictates the formation and spatial arrangement of FG and CG regions. Areas with low nuclei density tend to develop into CG regions, whereas those with high nuclei density evolve into FG regions. Such distinction arises from the two-stage nature of grain growth [43–45]. In the first stage, nuclei expand rapidly into the deformed matrix to reduce stored energy, driving fast grain boundary migration. Upon encountering neighboring grains, growth transitions to a second stage dominated by interfacial energy minimization, drastically slowing the growth rate—by a factor of 200–2000 [27]. Consequently, grains in high-nuclei-density regions quickly enter the slow-growth regime, producing FG regions, whereas those in low-nuclei-density regions experience extended growth, leading

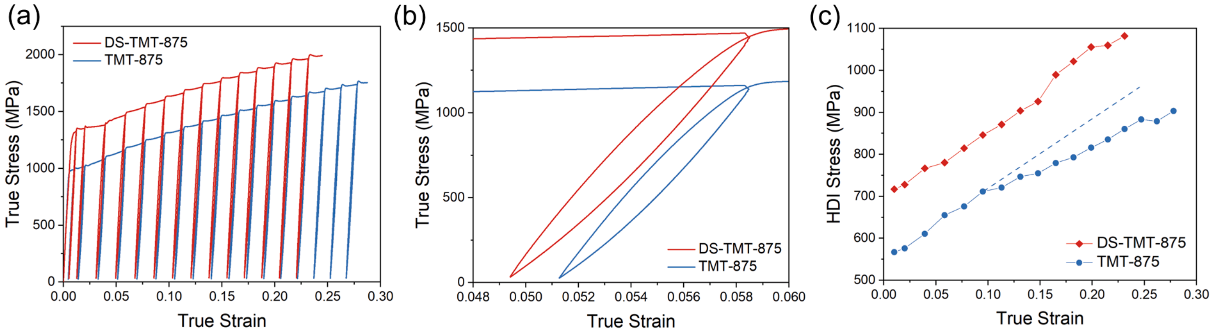

Fig. 6. (a) True stress-true strain curves of VCoNi processed under different conditions using LUR tensile tests; (b) Magnified unloading-reloading hysteresis loops taken from (a); (c) HDI stress derived from the unloading-reloading hysteresis loops.

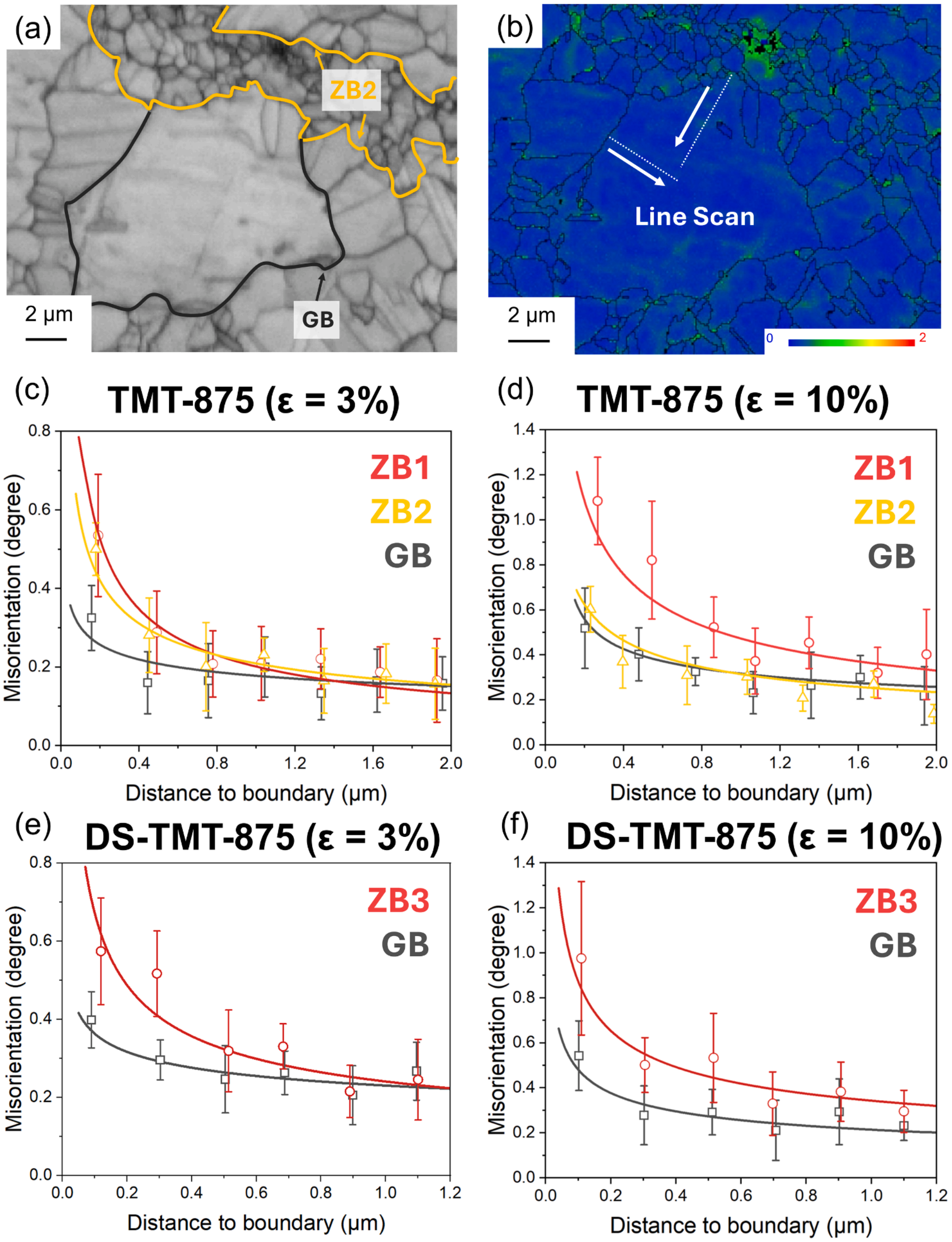

Fig. 7. Probing local evolution of HDI stress near different boundaries. (a) Band contrast image and (b) misorientation map of a grain in the CG region of TMT-875, illustrating how KAM line scans are conducted. (c–f) KAM profiles ahead of different boundaries: (c) TMT-875 after 3 % strain, (d) TMT-875 after 10 % strain, (e) DS-TMT-875 after 3 % strain, and (f) DS-TMT-875 after 10 % strain.

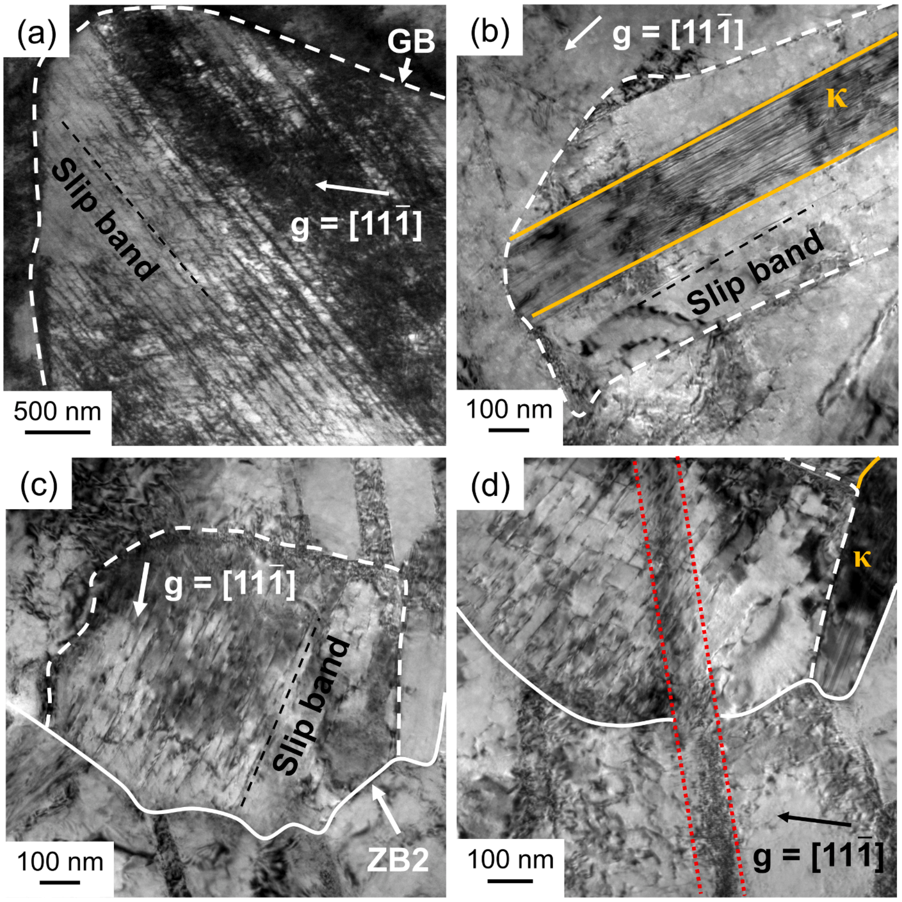

Fig. 8. (a–c) TEM images of representative grains in different regions of the TMT-875 sample after 10 % strain: (a) CG band; (b) FG band (HZ1); (c) FG sub-band (HZ2). (d) Propagation of a slip band across ZB2.

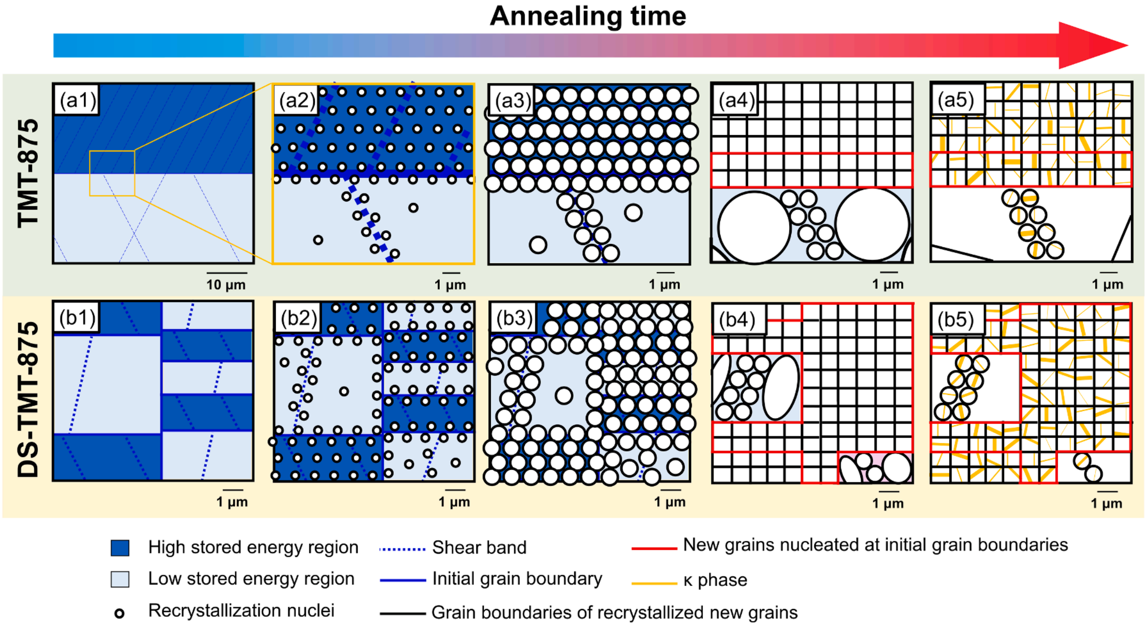

Fig. 9. Schematic illustration of microstructural evolution during annealing in (a1–a5) TMT-875 and (b1–b5) DS-TMT-875 samples, viewed along the transverse direction with rolling direction horizontal. Note the difference in magnification levels indicated by the scale bars. (a1, b1) show the as-rolled microstructures. (a2, b2) depict the spatial distribution of recrystallization nuclei, which form preferentially along shear bands, high-stored-energy grains, and initial grain boundaries. (a3–a4, b3–b4) illustrate grain growth and the formation of FG and CG regions, governed by the transition from stored-energy-driven growth to interface-energy-driven growth. (a5, b5) show the final microstructures, where FG regions promote κ-phase precipitation due to higher boundary density. Region and boundary annotations are explained in the legend.

to coarser grains. Therefore, by intentionally tailoring the distribution of nuclei, one can modulate the configuration of CG and FG regions.

Fig. 9 illustrates details of how refining the initial grain size influences the spatial distribution of recrystallization nuclei and the resulting heterostructure. In the TMT sample which has a coarse initial grain structure, cold rolling elongates these grains into bands tens to hundreds of microns thick (Fig. 9a1). Upon annealing, as shown in the magnified view in Fig. 9a2, recrystallization nuclei form preferentially in grains with high stored energy, along shear bands, and at initial grain boundaries, leading to regions with higher nucleation densities. In contrast, grains with lower stored energy generate significantly fewer nuclei. As annealing progresses (Figs. 9a3–4), new grains in high-nucleation-density regions rapidly encounter adjacent grains and results in the formation of FG bands or FG sub-bands. Meanwhile, in regions with sparse nuclei, new grains can continue growing for a longer duration before encountering each other, forming CG regions (Fig. 9a4). During subsequent annealing (Fig. 9a5), κ-phase precipitates preferentially within FG regions due to their high grain boundary density, which provides abundant heterogeneous nucleation sites. In contrast, CG regions—with their lower interfacial area and reduced boundary density—remain largely single-phased or contain only limited κ precipitates. Due to the sparse network of initial grain boundaries in the TMT-875 sample (see red box in Fig. 9a5), their contribution to FG zone formation is limited. As a result, their overall impact on nucleation is minor compared to that of the abundant nuclei formed along shear bands and in grains with high stored energy.

In contrast, the DS-TMT sample has an initial grain size approximately 1/28 that of the TMT sample. After cold rolling, the elongated grains in the DS-TMT sample are only 1–7 μm thick (Fig. 9b1). Consequently, their GBs form a network with an extremely high areal density, making them the dominant nucleation sites during annealing (Fig. 9b2). The small spacing between GBs ensures that most newly formed grains quickly encounter neighboring new grains and transition into the slow-growth stage, regardless of the stored energy of individual grains or the presence of shear bands (Fig. 9b3–b5). This results in the formation of an FG matrix in the DS-TMT sample (red box in Fig. 9b5). Only relatively large initial grains are capable of forming elongated grains with greater thickness, which provide more space for recrystallized grains to grow before encountering. These grains eventually develop into the CG lamellae (see Fig. 9b4). This formation mechanism inherently limits the size of the soft-zones and promotes their uniform distribution due to natural statistical variability in initial grain size—only a limited number of larger grains exist, and they tend to be evenly dispersed.

4.2. Origins of strength–ductility synergy in the ideal hetero-lamella structure

Refining the initial grain size with DS-TMT aligns the microstructure with the ideal HL structure design, achieving a superior strength–ductility synergy: a remarkable increase in strength while maintaining nearly the same elongation as that of the TMT sample. Specifically, the yield strength of DS-TMT-875 (1359 MPa) is 30 % higher than that of TMT-875 (1044 MPa), whereas their uniform elongations remain comparable (27 % vs. 31 %).

The higher yield strength of DS-TMT-875 can be understood by analyzing the strengthening mechanisms in these alloys. The total yield strength (σ_y) of a heterostructured alloy can be expressed as [4]:

$$\sigma_y = \sigma_{ROM} + \sigma_{HS},$$

where σ_{ROM} is the rule-of-mixtures (ROM) component, and σ_{HS} denotes the additional contribution arising from the heterostructure effect [5]. The ROM term can be written as:

$$\sigma_{ROM} = \sigma_{SZ} V_{SZ} + \sigma_{HZ} V_{HZ},$$

where σ_{SZ} and σ_{HZ} are the strengths, and V_{SZ} and V_{HZ} are the corresponding volume fractions, of the soft- and hard-zones, respectively. The relative volume fractions V_{SZ} and V_{HZ} directly influence σ_{ROM} via their weightings.

The soft-zone strength at yielding can be estimated as:

$$\sigma_{SZ} = \sigma_0 + \sigma_{gb} + \sigma_{ppt},$$

where σ_0 is the friction stress, σ_{gb} is the Hall–Petch strengthening, and σ_{ppt} is the precipitation strengthening. For VCoNi, $\sigma_0 = 383$ MPa [32]. σ_{gb} can be estimated by $\sigma_{gb} = k_{HP}\ d^{-1/2}$, where k_{HP} is the Hall–Petch slope (864 MPa·$\mu m^{1/2}$ for VCoNi [32]) and d is the average grain size in the soft-zone. Using the measured soft-zone grain sizes of 7.8 μm (TMT-875) and 2.7 μm (DS-TMT-875), their σ_{gb} are 309 MPa and 526 MPa, respectively. Because κ precipitates occupy only ~5 % and ~2 % of the total volume in TMT-875 and DS-TMT-875, their effect on yielding is negligible. Therefore, the estimated σ_{SZ} values are 692 MPa for TMT-875 and 909 MPa for DS-TMT-875.

The hard-zone strength is estimated using a similar relation:

$$\sigma_{HZ} = \sigma_0 + \sigma_{gb} + \sigma_{ppt},$$

However, the latter two terms should be treated jointly because the κ precipitates in the FG regions effectively act as grain refiners rather than conventional precipitation-strengthening agents. In both samples, the κ phase forms plate-like precipitates that penetrate through the FCC grains, creating dual-phase grains. Their large thickness (~200 nm) makes them non-shearable at yielding [35]. Moreover, the edges of these plates are directly connected to grain boundaries, leaving no free space for dislocations to bypass via the Orowan looping mechanism. Consequently, the strengthening contribution arises primarily from the subdivision of FCC grains into smaller domains, which can be represented by an effective grain size (d_{eff}) that accounts for both the true grain size and the subdividing effect of the κ plates. Using $d_{eff} = 0.754$ μm for TMT-875 and 0.937 μm for DS-TMT-875, the corresponding $\sigma_{gb,\ eff}$ values are estimated to be 995 MPa and 893 MPa, respectively. Therefore, the estimated σ_{HZ} values are 1378 MPa for TMT-875 and 1276 MPa for DS-TMT-875.

Based on the above analysis, the evidently higher strength of DS-TMT-875 can be attributed to two primary factors: (1) the increased hard-zone fraction (from 35 % to 65 %), which elevates the weighting of σ_{HZ} in σ_{ROM}; and (2) the pronounced increase in soft-zone strength (~200 MPa) through grain refinement, reflected by a larger σ_{gb} in σ_{SZ}. In addition, there exists an apparent discrepancy of approximately 100–200 MPa between the calculated σ_{ROM} (932 MPa for TMT-875 and 1147 MPa for DS-TMT-875) and the experimental σ_y (1044 MPa and 1359 MPa, respectively). This difference is reasonably attributed to σ_{HS}, which arises from heterostructure-induced long range back stress and the accumulation of additional GNDs near hetero-zone boundaries [4]. It should be noted that recent studies have shown that directly adding the HDI stress measured from LUR tests to the yield strength can lead to significant overestimation [46]. This is because σ_{HDI} comprises two components, of which only the Type II back stress—generated exclusively by heterostructure effects (i.e., σ_{HS})—is applicable to the yield strength. Unfortunately, direct estimation of the Type II back stress is nearly impossible for HSMs prepared by the R–R process used in this study.

Let us now turn to the discussion of ductility. In the present alloys, the CG regions are expected to exhibit a higher strain-hardening capacity than the FG regions, because the latter contain a relatively large κ fraction (29–36 %, Table 2) that is not readily hardenable. Thus, if only the volume-fraction effect is considered, the higher hard-zone (FG) fraction in DS-TMT-875 (~65 % FG) should enhance strength but reduce elongation compared with TMT-875 (~35 % FG). However, both samples show nearly identical strain-hardening behavior (Fig. 2c), suggesting that an additional hardening mechanism compensates for the reduced CG fraction. This compensation most likely originates from the refinement of the soft zones in DS-TMT-875. The smaller soft zones produce a higher density of zone boundaries per unit volume. As shown in Table 3, the boundary density in DS-TMT-875 (8.8×10^{-2} μm^{-2}) is approximately 28 % higher than that in TMT-875 (6.9×10^{-2} μm^{-2}), owing to the reduced dimensions of the soft zones. These hetero-interfaces create localized strain gradients due to the mismatches in strength and deformability between adjacent zones. To accommodate such gradients, large populations of GNDs accumulate near the interfaces, giving rise to additional strain-hardening through HDI effects [2,5].

Furthermore, the improved soft-zone uniformity in DS-TMT-875 is expected to suppress strain localization and thereby preserve high ductility. In the TMT-875 sample, the soft-zones are often separated by huge areas of hard-zones, and the distance between adjacent soft-zones is typically nearly 100 μm wide. By contrast, in the DS-TMT sample, refined initial grain size leads to the formation of fine and uniformly distributed soft lamellae, with an average spacing of only ~10 μm. This difference results from the refined initial grain structure and leads to a more homogeneous dispersion of deformable soft-zones. Embedding dispersed soft regions within a stronger or more brittle matrix is a long-standing strategy to improve ductility and damage tolerance, predating the development of HSMs [47–51]. This principle is well exemplified in bulk metallic glasses (BMGs), where introducing ductile BCC dendrites into Zr–Ti–Cu–Ni–Be glass matrix significantly enhances plasticity [47]. These ductile regions act as barriers to shear band propagation, promoting the activation of multiple, intersecting shear bands and reducing strain localization. A similar mechanism operates in HSMs, albeit with less abrupt strength gradients between soft- and hard-zones. Nonetheless, a more uniform distribution of soft-zones helps stabilize the local strain field, suppressing the development of dominant shear paths and instead encouraging multi-directional, dispersed shear band development [10,52]. For example, in partially recrystallized heterostructured Cu, microscale digital image correlation observations revealed that shear bands were frequently blocked near zone boundaries [10]. Even when shear bands penetrate into coarse-grained regions, their strain intensity is attenuated, suggesting that coarse grains help dissipate stress concentrations and regulate deformation behavior. Analogously, the uniformly distributed soft lamellae in DS-TMT-875 are expected to promote distributed plasticity and enhance strain stability, which in turn improves ductility.

4.3. *Unequal efficacy of hetero-zone boundaries: The critical role of hard-zone thickness*

An intriguing finding in this study is that not all hetero-zone boundaries contribute equally to HDI strengthening, particularly as deformation progresses (see Sec. 3.5). In the TMT-875 sample, two types of zone boundaries are present: ZB1, located between the soft-zone and the FG band (HZ1), and ZB2, located between the soft-zone and the FG sub-band (HZ2). At 3 % strain, KAM profiles reveal elevated GND densities near both ZB1 and ZB2 compared to regular GBs, confirming active HDI effects at these interfaces (Fig. 7). However, at 10 % strain, their behaviors diverge. The KAM level near ZB1 continues to rise, indicating a sustained HDI effect, whereas the KAM level near ZB2 saturates and becomes indistinguishable from that of ordinary GBs. This suggests that ZB2 loses its capacity to sustain strain incompatibility, resulting in the degradation of the HDI effect.

This degradation is closely associated with the pronounced deformation of HZ2 at higher strains. As shown in Fig. 8, when the global strain reaches 10 %, HZ1 and HZ2 exhibit markedly different internal strain states. While HZ1 maintains its hard-zone character with lower dislocation activity, HZ2 displays intense planar slip and a high density of slip bands, resembling the deformation microstructure of the surrounding soft matrix. As HZ2 increasingly accommodates strain, the mismatch in plastic deformation between HZ2 and the adjacent soft-zone diminishes. Consequently, the strain incompatibility across ZB2 decreases, leading to reduced GND accumulation and a decline in HDI hardening. Ultimately, the increased deformation at higher strain renders ZB2 equivalent to a regular GB, resulting in the loss of HDI effects.

Table 3
Densities of each zone boundary types in TMT-875 and DS-TMT-875 samples.

Sample	Zone boundary type	Density (μm^{-2})
TMT-875	ZB1	0.038 ± 0.011
	ZB2	0.031 ± 0.008
	ZB1+ZB2	0.069 ± 0.016
DS-TMT-875	ZB3	0.088 ± 0.021

The more pronounced deformation of HZ2 compared to HZ1 at higher global strain reveals an unanticipated yet important finding, which establishes a new geometrical constraint in HL structure design: hard-zones should maintain sufficient thickness to preserve HDI efficacy under high strain. This behavior can be rationalized from multiple perspectives. At the microscopic level, it is well established that forward stress develops at the heteto-interface on the hard-zone side, superimposing on the externally applied stress and promoting localized deformation within the hard-zone [3,5]. In relatively thin hard-zones such as HZ2, this HBAR occupies a larger fraction the zone's volume, thereby increasing the likelihood of plastic deformation. This interpretation is supported by TEM observations, where slip band propagation across ZB2 is visible in multiple locations (Fig. 8d shows one example). This suggests that the dislocation pile-up from adjacent soft-zone has induced dislocation activity within the hard-zone. In other words, the mechanical barrier function of ZB2 has degraded, allowing interfacial slip transmission to occur.

From a mesoscopic standpoint, during deformation the soft-zones undergo much larger plastic deformation than the hard-zones, resulting in non-uniform strain distributions surrounding the latter [12,53]. These strain fields impose additional mechanical loading on the hard-zones. However, owing to its larger cross-sectional area, the thicker HZ1 can more effectively distribute these forces, resulting in lower stress per unit area and delayed yielding. Conversely, the thinner HZ2, with its smaller load-bearing area, experiences higher local stresses, leading to earlier yielding and greater deformation. From a macroscopic perspective, the hard-zone can be viewed as a structural element whose resistance to bending or deformation is governed by its structural stiffness, defined as EI, where E is Young's modulus and I is the area moment of inertia [54]. For a rectangular cross-section, I is proportional to the cube of the thickness ($I \propto h^3$), meaning even modest increases in thickness result in a significant enhancement of structural stiffness. Therefore, HZ1, being considerably thicker than HZ2, possesses much greater resistance to bending deformation, further explaining its lower strain accumulation under applied load.

Traditionally, heterostructure design has placed greater emphasis on tailoring the soft-zones—such as their size, geometry and distribution [4,6]. In contrast, hard-zones has received far less attention. The present findings reveal the key role of hard-zone geometry in sustaining HDI effects under large strains. It is worth noting that such thin, elongated hard-zones are not unique to VCoNi [55], but is commonly reported in R–R processed alloys, such as Mg alloys [56–58] and Fe alloys [59–62]. This suggests that the mechanical degradation of ZB2 and the critical role of hard-zone thickness are not isolated phenomena, but may be broadly relevant across different classes of HSMs.

5. Conclusions

This study establishes initial grain size engineering as an effective strategy for realizing hetero-lamella structure and exceptional strength–ductility synergy in HSMs fabricated by the R–R process. The effectiveness of the strategy is demonstrated in a VCoNi medium-entropy alloy, where the initial grain size is deliberately refined through a dual-stage thermomechanical treatment. The major findings are summarized as follows:

1. Initial grain size refinement transforms a coarse, irregular banded heterostructure into a near-ideal HL structure, featuring lamella-shaped soft-zones uniformly embedded in a hard-zone matrix. This results in four key microstructural improvements: increased hard-zone fraction, refined grain size, substantial reduction in soft-zone size, and improved soft-zone spatial uniformity.
2. Refinement of initial grain size increases grain boundary spatial density by several hundreds of times and shifts the dominant nucleation-site distribution mechanism to be near exclusively grain-boundary-controlled. This new recrystallization pathway promotes dense, uniformly distributed nucleation, leading to a fine-grained matrix. It also inherently limits soft-zone dimensions and enhances soft-zone spatial uniformity.
3. The resulting hetero-lamella structure in DS-TMT-875 achieves a yield strength of 1.36 GPa, an ultimate tensile strength of 1.61 GPa, and a uniform elongation of 27 %, representing a 315 MPa gain in strength with only a 4 % loss in uniform elongation compared to TMT-875. This demonstrates a remarkable strength–ductility synergy, far superior to that attainable from a coarse-grained initial material.
4. The improved mechanical properties stem from multiple synergistic mechanisms. The increased hard-zone volume fraction and refined grain size raise strength, while the reduced size and uniform distribution of soft-zones enhance HDI strain hardening and deformation stability, preserving ductility.
5. Localized KAM and TEM analyses reveal for the first time that hetero-zone boundary efficacy depends strongly on hard-zone thickness. Boundaries adjacent to thin hard-zones lose strain incompatibility at high strain, losing their contributions to HDI effects. This finding identifies hard-zone thickness as a previously overlooked but critical geometric parameter in heterostructure design, essential for sustaining HDI effects under large strains.
6. Finally, this study identifies initial grain size engineering as a critical new dimension to optimize the hetero-architecture in the R–R process. It enables direct control over soft-zone dimension and uniformity, which is almost unattainable in traditional approaches that rely solely on thermal or mechanical tuning. This insight opens new opportunities for the development of next-generation heterostructured alloys with unprecedented combinations of strength and ductility.

CRediT authorship contribution statement

Shu-Yi Tung: Data curation, Formal analysis, Investigation, Methodology, Writing – original draft, Conceptualization. **Yi-Chia Chen:** Data curation, Investigation. **Yuntian Zhu:** Writing – review & editing. **Ming-Hung Tsai:** Conceptualization, Supervision, Writing – review & editing, Methodology.

Declaration of competing interest

The authors declare that they have no known competing financial interests or personal relationships that could have appeared to influence the work reported in this paper.

Acknowledgements

This work was financially supported by the “High Entropy Materials Center” from the Featured Areas Research Center Program within the framework of the Higher Education Sprout Project by the Ministry of Education (MOE), Taiwan. This work is also supported by the National Science and Technology Council, Taiwan (under grant NSTC 114-2221-E-005-053-MY3). The authors thank the Instrument Center of National Chung Hsing University for the help on EBSD analysis.

Supplementary materials

Supplementary material associated with this article can be found, in the online version, at doi:10.1016/j.actamat.2025.121675.

References

[1] X. Dong, B. Gao, L. Xiao, J. Hu, M. Xu, Z. Li, J. Meng, X. Han, H. Zhou, Y. Zhu, Heterostructured metallic structural materials: research methods, properties, and future perspectives, Adv. Funct. Mater. 34 (51) (2024) 2410521.

[2] X. Wu, Y. Zhu, Heterogeneous materials: a new class of materials with unprecedented mechanical properties, Mater. Res. Lett. 5 (8) (2017) 527–532.

[3] Y. Zhu, X. Wu, Heterostructured materials, Prog. Mater. Sci. 131 (2023) 101019.

[4] Y. Wang, Y. Zhu, Z. Yu, J. Zhao, Y. Wei, Hetero-zone boundary affected region: a primary microstructural factor controlling extra work hardening in heterostructure, Acta Mater. 241 (2022) 118395.

[5] Y. Zhu, X. Wu, Perspective on hetero-deformation induced (HDI) hardening and back stress, Mater. Res. Lett. 7 (10) (2019) 393–398.

[6] Y. Zhu, K. Ameyama, P.M. Anderson, I.J. Beyerlein, H. Gao, H.S. Kim, E. Lavernia, S. Mathaudhu, H. Mughrabi, R.O. Ritchie, Heterostructured materials: superior properties from hetero-zone interaction, Mater. Res. Lett. 9 (1) (2021) 1–31.

[7] C. Huang, Y. Wang, X. Ma, S. Yin, H. Höppel, M. Göken, X. Wu, H. Gao, Y. Zhu, Interface affected zone for optimal strength and ductility in heterogeneous laminate, Mater. Today 21 (7) (2018) 713–719.

[8] H. Ran, W. Su, P. Ye, X. Chen, C. Zhang, Q. Cheng, Q. Wang, X. Lu, C. Huang, Synergistic deformation mechanisms in Cu–Fe layered materials: a strain gradient plasticity finite element analysis, J. Mater. Res. Technol. 29 (2024) 5000–5009.

[9] H. Ran, P. Ye, F. Guo, M. Wang, W. Su, X. Chen, S. Gao, N. Tsuji, Y. Zhu, X. Lu, Superior strength-ductility combination resulted from hetero-zone boundary affected region in Cu-Fe layered material, J. Mater. Res. Technol. 181 (2024) 209–219.

[10] Y. Wang, C. Huang, Q. He, F. Guo, M. Wang, L. Song, Y. Zhu, Heterostructure induced dispersive shear bands in heterostructured Cu, Scr. Mater. 170 (2019) 76–80.

[11] F. Liang, B. Zhang, Y. Yong, X.-M. Luo, G.-P. Zhang, Enhanced strain delocalization through formation of dispersive micro shear bands in laminated Ni, Int. J. Plast 132 (2020) 102745.

[12] X. Wu, M. Yang, F. Yuan, G. Wu, Y. Wei, X. Huang, Y. Zhu, Heterogeneous lamella structure unites ultrafine-grain strength with coarse-grain ductility, Proc. Natl. Acad. Sci. U.S.A 112 (47) (2015) 14501–14505.

[13] Y. Wang, X. Zhang, T. Chen, Heterogeneous lamella structure design to simultaneously strengthen and toughen aluminum alloys, J. Alloys Compd. 930 (2023) 167456.

[14] X. Zhang, Y. Wang, T. Chen, Utilizing powder thixoforming to fabricate heterogeneous lamella structure in aluminum alloy: Formation, strengthening and toughening mechanisms, Mater. Sci. Eng. A 883 (2023) 145518.

[15] K. Liu, Q. Cui, L. Shi, J. Yang, Y. Cai, Y. Su, Q. Ouyang, D. Zhang, Grain structure tailoring strategy for heterogeneous lamella SiCp/2024Al composites with exceptional strength-ductility synergy, Compos. B: Eng. 280 (2024) 111491.

[16] S. Li, X. Luo, Z. Sun, H. Zhou, S. Xiong, B. Liu, L. Zeng, B. Yang, Construction of a dual heterogeneous lamella structure to improve the electrical conductivity and mechanical properties of Cu alloys, Mater. Lett. 338 (2023) 134016.

[17] J. Fan, X. Ji, L. Fu, J. Wang, S. Ma, Y. Sun, M. Wen, A. Shan, Achieving exceptional strength-ductility synergy in a complex-concentrated alloy via architected heterogeneous grains and nano-sized precipitates, Int. J. Plast 157 (2022) 103398.

[18] C. Zhang, Q. Yu, Y.T. Tang, M. Xu, H. Wang, C. Zhu, J. Ell, S. Zhao, B. E. MacDonald, P. Cao, Strong and ductile FeNiCoAl-based high-entropy alloys for cryogenic to elevated temperature multifunctional applications, Acta Mater. 242 (2023) 118449.

[19] K. Wang, F. Qi, D. Liu, S. Ma, L. Fu, A. Shan, Achieving excellent mechanical and electrical properties in Al-Si alloy via heterogeneous lamella structure with high-density nanoprecipitates, Mater. Sci. Eng. A 924 (2025) 147778.

[20] X. Liu, K. Vecchio, Simultaneously improving mechanical and magnetic properties through heterogeneous lamella structures in a superalloy-like, soft magnetic complex concentrated alloy, Mater. Res. Lett. 11 (9) (2023) 749–756.

[21] H. Jiang, H. Xing, Z. Xu, J. Feng, J. Zhang, B. Sun, Achieving superior strength-ductility balance in novel heterogeneous lamella structures of Al-Zn-Mg-Cu alloys, J. Mater. Res. Technol. 184 (2024) 122–135.

[22] X. Liu, S. Zhang, H. Feng, J. Wang, P. Jiang, H. Li, F. Yuan, X. Wu, Outstanding fracture toughness combines gigapascal yield strength in an N-doped heterostructured medium-entropy alloy, Acta Mater. 255 (2023) 119079.

[23] H. Yang, M. Zhu, N. Chen, S. Xie, Y. Yu, G. Wang, C. Wang, H. Kou, Novel hierarchical α structure enhanced strength-ductility synergy in metastable β titanium alloy, Mater. Sci. Eng. A 925 (2025) 147877.

[24] L. Xie, T. Huang, L. Zhang, W. Cao, G. Wu, X. Huang, Managing both strength and ductility in duplex stainless steel with heterogeneous lamella structure, Mater. Sci. Eng. A 738 (2018) 190–193.

[25] G. Niu, H. Wu, D. Zhang, N. Gong, D. Tang, Heterogeneous nano/ultrafine-grained medium Mn austenitic stainless steel with high strength and ductility, Mater. Sci. Eng. A 725 (2018) 187–195.

[26] D. Zhang, H. Zhang, J. Zhu, M. Ding, X. An, D. Wu, W. Hu, T. Yang, High strength-ductility synergy of Inconel 625 alloy with a layered bimodal grain-structure, Mater. Charact. 207 (2024) 113510.

[27] A. Rollett, G.S. Rohrer, J. Humphreys, Recrystallization and Related Annealing Phenomena, 3rd ed., Elsevier, 2017.

[28] R. Zhou, J. Yan, H. Tao, X. Ma, X. Liang, Y. Liu, Y. Zhu, Moderate rolling for producing effective heterostructure, Scr. Mater. 253 (2024) 116289.

[29] Y. Yang, Y. Liu, S. Yan, S. Jiang, Z. He, H. Pan, N. Jia, On the micromechanism of superior strength and ductility synergy in a heterostructured Mg-2.77 Y alloy, J. Magnes. Alloys 12 (7) (2024) 2793–2811.

[30] L. Zhang, K. Song, X. Zhang, C. Ma, X. Hai, Heterogeneous structure design and strengthening mechanism study of 2205 duplex stainless steel, Mater. Today Commun. 42 (2025) 111481.

[31] P. Sathiyamoorthi, P. Asghari-Rad, J.W. Bae, H.S. Kim, Fine tuning of tensile properties in CrCoNi medium entropy alloy through cold rolling and annealing, Intermetallics 113 (2019) 106578.

[32] S.S. Sohn, A. Kwiatkowski da Silva, Y. Ikeda, F. Körmann, W. Lu, W.S. Choi, B. Gault, D. Ponge, J. Neugebauer, D. Raabe, Ultrastrong medium-entropy single-phase alloys designed via severe lattice distortion, Adv. Mater. 31 (8) (2019) 1807142.

[33] J.M. Park, D.C. Yang, H.-J. Kim, D.G. Kim, S. Lee, H.S. Kim, S.S. Sohn, Ultra-strong and strain-hardenable ultrafine-grained medium-entropy alloy via enhanced grain-boundary strengthening, Mater. Res. Lett. 9 (7) (2021) 315–321.

[34] D.C. Yang, Y.H. Jo, Y. Ikeda, F. Körmann, S.S. Sohn, Effects of cryogenic temperature on tensile and impact properties in a medium-entropy VCoNi alloy, J. Mater. Res. Technol. 90 (2021) 159–167.

[35] F. An, J. Hou, J. Liu, B. Qian, W. Lu, Deformable κ phase induced deformation twins in a CoNiV medium entropy alloy, Int. J. Plast. 160 (2023) 103509.

[36] T. Chou, W. Li, Y. Zhou, J. Zhang, J. Ju, Y. Zhao, Y. Wang, Y. Zhao, F. Chen, X. Wang, A novel Widmanstätten-patterned multicomponent alloy: κ-strengthened VCoNi medium-entropy alloy, Scr. Mater. 258 (2025) 116495.

[37] B. Xu, H. Duan, X. Chen, J. Wang, Y. Ma, P. Jiang, F. Yuan, Y. Wang, Y. Ren, K. Du, Harnessing instability for work hardening in multi-principal element alloys, Nat. Mater. 23 (6) (2024) 755–761.

[38] C. Liu, H. Inouye, Control of ordered structure and ductility of (Fe, Co, Ni) 3 V alloys, Met. Trans. A 10 (1979) 1515–1525.

[39] C. Liu, Atomic ordering and structural transformation in the V-Co-Ni ternary alloys, Metall. Trans. 4 (1973) 1743–1753.

[40] S.S. Sohn, D.G. Kim, Y.H. Jo, A.K. da Silva, W. Lu, A.J. Breen, B. Gault, D. Ponge, High-rate superplasticity in an equiatomic medium-entropy VCoNi alloy enabled through dynamic recrystallization of a duplex microstructure of ordered phases, Acta Mater. 194 (2020) 106–117.

[41] M. Yang, Y. Pan, F. Yuan, Y. Zhu, X. Wu, Back stress strengthening and strain hardening in gradient structure, Mater. Res. Lett. 4 (3) (2016) 145–151.

[42] X.W.H. Zhou, D. Srolovitz, Y. Zhu, Defining and designing heterostructured materials, Nat. Mater. (2025). In press.

[43] Y. Huang, F. Humphreys, Subgrain growth and low angle boundary mobility in aluminium crystals of orientation {110}<001>, Acta Mater. 48 (8) (2000) 2017–2030.

[44] M. Somerday, F. Humphreys, Recrystallisation behaviour of supersaturated al–mn alloys part 1–al–1.3 wt-% mn, Mater. Sci. Technol. 19 (1) (2003) 20–29.

[45] M. Somerday, F. Humphreys, Recrystallisation behaviour of supersaturated Al–Mn alloys Part 2–Al–0.3 wt-% Mn, Mater. Sci. Technol. 19 (1) (2003) 30–35.

[46] E. Ma, T. Zhu, Defining structural gradient hardening through Type II back stress for heterostructured materials, Scr. Mater. (2025) 116995.

[47] C. Hays, C. Kim, W.L. Johnson, Microstructure controlled shear band pattern formation and enhanced plasticity of bulk metallic glasses containing in situ formed ductile phase dendrite dispersions, Phys. Rev. Lett. 84 (13) (2000) 2901.

[48] D.C. Hofmann, J.-Y. Suh, A. Wiest, G. Duan, M.-L. Lind, M.D. Demetriou, W. L. Johnson, Designing metallic glass matrix composites with high toughness and tensile ductility, Nature 451 (7182) (2008) 1085–1089.

[49] D.C. Hofmann, J.-Y. Suh, A. Wiest, M.-L. Lind, M.D. Demetriou, W.L. Johnson, Development of tough, low-density titanium-based bulk metallic glass matrix composites with tensile ductility, Proc. Natl. Acad. Sci. U.S.A 105 (51) (2008) 20136–20140.

[50] Y. Wu, Y. Xiao, G. Chen, C.T. Liu, Z. Lu, Bulk metallic glass composites with transformationmediated work-hardening and ductility, Adv. Mater. 22 (25) (2010) 2770–2773.

[51] Y. Wu, H. Wang, H. Wu, Z. Zhang, X. Hui, G. Chen, D. Ma, X. Wang, Z. Lu, Formation of Cu–Zr–Al bulk metallic glass composites with improved tensile properties, Acta Mater. 59 (8) (2011) 2928–2936.

[52] Y. Wang, C. Huang, Y. Li, F. Guo, Q. He, M. Wang, X. Wu, R.O. Scattergood, Y. Zhu, Dense dispersed shear bands in gradient-structured Ni, Int. J. Plast. 124 (2020) 186–198.

[53] H.K. Park, K. Ameyama, J. Yoo, H. Hwang, H.S. Kim, Additional hardening in harmonic structured materials by strain partitioning and back stress, Mater. Res. Lett. 6 (5) (2018) 261–267.

[54] F.A. Leckie, D.J. Bello, Strength and stiffness of engineering systems, Springer Science & Business Media, 2009.

[55] C. Zhang, C. Zhu, P. Cao, X. Wang, F. Ye, K. Kaufmann, L. Casalena, B. E. MacDonald, X. Pan, K. Vecchio, Aged metastable high-entropy alloys with heterogeneous lamella structure for superior strength-ductility synergy, Acta Mater. 199 (2020) 602–612.

[56] X. Liu, B. Zhu, F. Wei, W. Yang, W. Liu, L. Li, C. Xu, P. Guo, Heterogeneous lamella mixed grain structures of strength-ductility synergy in medium strain rate rolled AZ31 magnesium sheets, Mater. Sci. Eng. A 916 (2024) 147387.

[57] T. Wang, M. Zha, C. Du, H.-L. Jia, C. Wang, K. Guan, Y. Gao, H.-Y. Wang, High strength and high ductility achieved in a heterogeneous lamella-structured magnesium alloy, Mater. Res. Lett. 11 (3) (2023) 187–195.

[58] X. Wang, W. Liu, X. Hu, K. Wu, Microstructural modification and strength enhancement by SiC nanoparticles in AZ31 magnesium alloy during hot rolling, Mater. Sci. Eng. A 715 (2018) 49–61.

[59] J. Wang, S. Zhang, W. Wang, X. Wu, F. Yuan, Enhanced fracture properties by heterogeneous grain structures and dual nanoprecipitates, Intermetallics 180 (2025) 108707.

[60] X. Qiu, Y. Wang, K. Zeng, J. He, C. Gao, Z. Xiong, X. Cheng, Achieving a superior combination of strength and ductility by adjusting heterogeneous structure in a Fe–Mn–Al–Mo–C lightweight steel, Mater. Sci. Eng. A 913 (2024) 147078.

[61] H. Zhu, Q. Gao, Y. Zou, H. Ding, Achieving strength ductility synergy of multiple hetero-structured Fe–24Mn–10Al–1C duplex lightweight steel, Mater. Sci. Eng. A 922 (2025) 147651.

[62] J. Li, B. Gao, Z. Huang, H. Zhou, Q. Mao, Y. Li, Design for strength-ductility synergy of 316L stainless steel with heterogeneous lamella structure through medium cold rolling and annealing, Vacuum 157 (2018) 128–135.